

Retraction

Retracted: NECScanNet: Novel Method for Cervical Neuroendocrine Cancer Screening from Whole Slide Images

Security and Communication Networks

Received 26 December 2023; Accepted 26 December 2023; Published 29 December 2023

Copyright © 2023 Security and Communication Networks. This is an open access article distributed under the Creative Commons Attribution License, which permits unrestricted use, distribution, and reproduction in any medium, provided the original work is properly cited.

This article has been retracted by Hindawi, as publisher, following an investigation undertaken by the publisher [1]. This investigation has uncovered evidence of systematic manipulation of the publication and peer-review process. We cannot, therefore, vouch for the reliability or integrity of this article.

Please note that this notice is intended solely to alert readers that the peer-review process of this article has been compromised.

Wiley and Hindawi regret that the usual quality checks did not identify these issues before publication and have since put additional measures in place to safeguard research integrity.

We wish to credit our Research Integrity and Research Publishing teams and anonymous and named external researchers and research integrity experts for contributing to this investigation.

The corresponding author, as the representative of all authors, has been given the opportunity to register their agreement or disagreement to this retraction. We have kept a record of any response received.

References

- [1] X. Liao, Q. Huang, and X. Zheng, “NECScanNet: Novel Method for Cervical Neuroendocrine Cancer Screening from Whole Slide Images,” *Security and Communication Networks*, vol. 2021, Article ID 5868501, 12 pages, 2021.

Research Article

NECScanNet: Novel Method for Cervical Neuroendocrine Cancer Screening from Whole Slide Images

Xin Liao ,¹ Qin Huang ,¹ and Xin Zheng ,²

¹Department of Pathology,

Key Laboratory of Birth Defects and Related Diseases of Women and Children (Sichuan University) Ministry of Education,
West China Second University Hospital of Sichuan University, Chengdu, China

²College of Computer Science and Engineering, University of Electronic Science and Technology of China, Chengdu 611731, China

Correspondence should be addressed to Qin Huang; zhonghuangqin@163.com and Xin Zheng; xin_zheng0311@uestc.edu.cn

Received 24 August 2021; Revised 24 September 2021; Accepted 13 October 2021; Published 31 October 2021

Academic Editor: Jian Su

Copyright © 2021 Xin Liao et al. This is an open access article distributed under the Creative Commons Attribution License, which permits unrestricted use, distribution, and reproduction in any medium, provided the original work is properly cited.

As a rare malignant tumor, cervical neuroendocrine cancer (NEC) is difficult in diagnosis even for experienced pathologists. A computer-assisted diagnosis may be helpful for the improvement of diagnostic accuracy. Nevertheless, the computer-aided pathological diagnosis has to face a great challenge that the hundred-million-pixels or even gig-pixels whole slide images (WSIs) cannot be applied directly in the existing deep convolution network for training and analysis. Therefore, the construction of a neural network to realize the automatic screening of cervical NEC is challenging; meanwhile, as far as we know, little attention has been paid to this field. In order to address this problem, here we present a multiple-instance learning method for automatic recognition of cervical NEC on pathological WSI, which consists of the Sliding Detector module and Lesion Analyzer module. A pathological WSI dataset, which is composed of 84 NEC cases and 216 NEC-free cases from the Pathological Department of West China Second University Hospital, is applied to evaluate the performance of the method. The experimental results show that the recall rate, accuracy rate, and precision rate of our method for automatic recognition are 92.9%, 92.7%, and 83.0%, respectively, demonstrating the effectiveness and the potential in clinical practice. The application of this method in computer-assisted pathological diagnosis is expected to decrease the misdiagnosis as well as the false diagnosis of rare cervical NEC, and, consequently, improve the therapeutic effect of cervical cancers.

1. Introduction

Cervical neuroendocrine carcinoma (NEC) is a rare malignancy, accounting for only 2% of cervical cancers [1]. NEC patients are typically diagnosed at younger ages than women with other common cervical carcinoma and with a higher frequency in Asian women [1, 2]. Cervical NEC is characterized by higher degree of malignancy, earlier distant metastasis, and worse prognosis compared with other cervical cancers [2]. Due to the rarity, there is no standardized treatment regimen; however, it has been proved that the application of ordinary treatment strategy for cervical squamous carcinoma and adenocarcinoma leads to extremely lower overall survival than that of the two common types of cervical cancers [2, 3]. In contrast, the treatment

regime for the lung small-cell carcinoma may have a better efficacy in cervical NEC [3]. Herein, the precise diagnosis of NEC is critical for the patients' benefits. However, the clinical symptoms, including vaginal bleeding, pelvic mass, vaginal bleeding, and abdominal pain, and the radiological imaging features of cervical NEC are both untypical, and the pathological diagnosis, which is the gold standard of it, is difficult even for experienced pathologists, because the morphology of NEC is diverse, and it often coexists with other cervical cancers, so the NEC lesions may be concealed by other lesions, leading to a high possibility of misdiagnosis and false diagnosis [3–5].

At present, deep learning has been recognized as an effective tool in the field of medicine, especially in medical image analysis [6, 7]. In the recent years, along with the

development of microphotography and whole slide scanning technology, the pathological slides can be preserved in the form of digital image, and the computer-aided diagnostic system based on the deep learning methods has been introduced into pathological field [7], demonstrating its advantages in both lesion detection [8, 9] and prognostic analysis [10, 11]. The deep convolution neural network (CNN), as a representative of deep learning method which is able to extract the image features automatically, has achieved great success in the field of computer vision technology [12, 13] and is expected to have superior performance in the field of computer-aided diagnosis to improve the diagnostic accuracy and efficiency [14, 15]. However, due to the extremely large size of pathological whole slide images (WSIs), the WSIs cannot be applied directly in most CNN models [16, 17], or the amount of computation and memory space required will exceed the capacity of mainstream GPU hardware in the emergence stage. Meanwhile, as images with detailed and complex features, the pixel-reduced pre-processing may lead to the loss of meaningful details in the cellular level. Therefore, in this paper, we aim to exploit a computer-assisted diagnostic method for the pathological diagnosis of cervical NEC based on the WSIs.

The rest of this paper is organized as follows. The relevant medical background and computer technology involved in this study are reviewed in Section 2. In Section 3, we present the methodology of the research. We present the experiments and results in Section 4. Section 5 is conclusion.

2. Related Work

In this section, the relevant medical background and computer technology are involved in our research, including computer-aided diagnosis based on the deep learning method and multi-instance learning technology.

2.1. Computer-Assisted Diagnosis via Deep Learning Methods. Computer-aided diagnosis (CAD) is defined to be computing models for a specific disease which can automatically localize and categorize the lesions and, even more, analyze the prognosis of the corresponding disease [18]. An ideal CAD system is capable of the precise intelligent analysis of medical images, providing the doctors with reference to assist diagnosis and treatment and, at the same time, improving the efficacy and accuracy of clinical practices. Driven by the continuous development of deep learning algorithm and graphics processing unit (GPU), CAD has also entered a new research stage. In the recent years, the deep learning technology has been applied in multiple fields which involve the CAD systems, focusing on the medical image analysis of computed tomography (CT) [19, 20], magnetic resonance imaging (MRI) [21, 22], X-ray [23], ultrasonic examination [24], endoscope [25], and pathological slides [26–29].

2.2. Neuroendocrine Carcinoma of the Cervix. NEC of the cervix is a rare malignant tumor. Although the incidence of this kind of tumor is low, it is prone to lymphatic and

hematogenous metastasis in the early stage, and its prognosis is significantly worse than that of cervical squamous cell carcinoma and adenocarcinoma in the same period [30]. The prognostic factors for NEC patients have not yet been determined, but most studies indicated that the main factors affecting the prognosis of NEC patients include clinical stage, tumor size, lymph node metastasis, and the efficacy of treatment; thus, the early and precise diagnosis of cervical NEC is quite significant to improve the prognosis [31]. However, the rate of misdiagnosis for NEC is considerably high even for specialist pathologists [31], raising the question whether a computer-assisted pathological diagnosis may be helpful to improve the accuracy of diagnosis [31]. Nevertheless, the automatic detection of NEC lesions by computer on WSI is quite challenging due to the extremely small amount of data and the unavailability of precisely labeled data due to the low prevalence of the tumor and the huge labor consumption of manual annotation.

2.3. Multiple-Instance Learning. Multiple-instance learning (MIL) is a weakly supervised learning, which establishes a multi-instance classifier by learning word bags with category labels and applies the classifier to the prediction of unknown word bags [32, 33]. The MIL has been applied in the pathological field for the WSI analysis [28, 34]. In this research, we utilize the MIL algorithm to realize the binary classification (NEC and NEC-free) on the WSIs. In details, the WSIs of NEC patients are composed of the NEC patches and NEC-free patches, while the WSIs of NEC-free patients merely consisted of NEC-free patches. It is postulated that there is at least one image patch with positive (NEC) label in the bags corresponding to the WSIs of NEC patients but none in the bags corresponding to the WSIs of NEC-free patients; herein, we can consider the NEC and NEC-free patients to be positive and negative bags and the NEC and NEC-free patches to be positive and negative instances, respectively. Therefore, the aforementioned binary classification can be explained by MIL algorithm; the binary classification MIL is demonstrated in Figure 1.

3. Materials and Methods

3.1. The NEC Dataset and System Set-Up. The NEC dataset was collected from West China Second University Hospital, Sichuan University. The dataset is composed of 84 NEC cases and 216 NEC-free cases from 2008 to 2016. All the cases involved in the research were reviewed by two experienced pathologists in double-blind way to confirm the diagnosis. On the basis of the World Health Organization (WHO) classification standard for female genital tumor, cervical neuroendocrine carcinoma is classified into low grade and high grade groups. The former group contains carcinoid and atypical carcinoid carcinoma, while the latter contains small-cell and large-cell neuroendocrine carcinoma. In our group, 76 cases (90.24%) were small-cell neuroendocrine carcinoma, 8 cases (9.76%) were large-cell neuroendocrine carcinoma, and no carcinoid carcinoma was

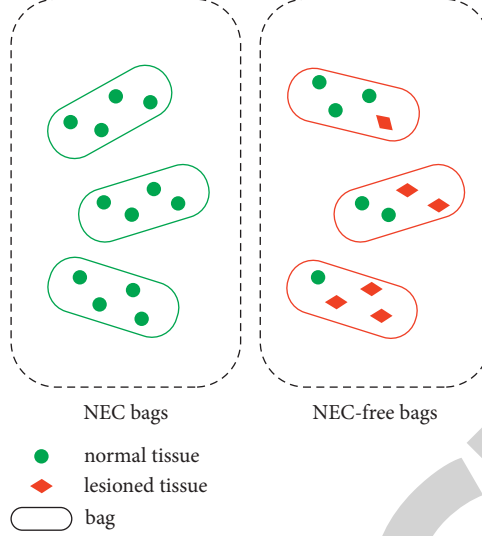


FIGURE 1: Binary classification MIL. NEC bags are generated from WSIs with NEC labels and NEC-free bags are generated from WSIs with NEC-free labels. Only the image patches of regions with a specific category, for example, image patches of tumor regions in NEC WSIs, are regarded as positive instances.

found. The typical cases and proportions of each category are demonstrated in Figure 2.

The surgical specimens from patients were fixed by 10% neutral formalin, and routine dehydration, paraffin embedding, 4 um thick serial sections and hematoxylin-eosin (H&E) staining were performed routinely to obtain pathological H&E slides. These slides were then scanned at a magnification of 20x (0.5 $\mu\text{m}/\text{pixel}$) by Motic®EasyScan system (Motic Electric Group Co., Ltd.) to achieve the high quality WSIs.

3.2. Proposed Method. The implementation process of NEC screening network, named NECSanNet, based on multi-instance deep learning method is as follows: in the first step, the WSI image is preprocessed to remove the blank background areas and interference areas, so that the stained tissue areas are obtained. Then, the suspected cancerous areas are detected from the stained tissue areas, followed by the prediction of the case label for the category probability according to the characteristics of the suspected cancerous areas. In details, in a given WSI image, the predicted probability that the corresponding case belongs to NEC category is as follows:

$$P(\hat{Y}_n = \text{NEC}) = \frac{p_{\text{NEC}}}{p_{\text{FREE}}} + p_{\text{NEC}}. \quad (1)$$

in which

$$p_{\text{NEC}} = \exp\left(\frac{1}{|\beta_n|} \sum_{b \in \beta_n} \log P(\hat{Y}_n = \text{NEC})\right), \quad (2)$$

$$p_{\text{FREE}} = \exp\left(\frac{1}{|\beta_n|} \sum_{b \in \beta_n} \log P(\hat{Y}_n = \text{FREE})\right),$$

where $P(\hat{Y}_n = \text{NEC})$ and $P(\hat{Y}_n = \text{FREE})$ represent the probability labels of NEC and NEC-free categories. The structure of the NECSanNet is demonstrated in Figure 3, which is composed of a sliding-window detected module named Sliding Detector (on the left side of Figure 3) and a lesion-analyzed module named Lesion Analyzer (on the right side of Figure 3).

(1) *The Sliding Detector Module.* $M_{\text{sliding}}(\theta_s): \{\text{WSI}\} \rightarrow \{\text{patch}_i\}$; the structure of network is shown in Figure 4, which is composed of two clarification networks, RESNET-50 and RESNET-INCEPTION-V2. In the Sliding Detector module, K_1 image blocks (K_1 value range 5–20, default value 10) with the highest possibilities to be tumor regions are detected from the stained tissue area by sliding-window sampling method, in which θ_M represents the set group of trainable parameters, and the feature vector of the image block is mapped to the category label probability of the image block.

(2) *The Lesion Analyzer Module.* $M_{\text{analyzer}}(\theta_a): \{\text{patch}_i\} \rightarrow P(\hat{Y}_b)$, which is a multiple-instance convolution network, and its structure is demonstrated in Figure 5. The network can predict the category labels (\hat{Y}_b) of cases according to the characteristics of suspected cancerous regions detected by Sliding Detector based on multi-instance deep learning method, in which character θ_a represent a set group of trainable parameters.

3.2.1. The Sliding Detector Module. The structure of network is shown in Figure 4, which can accomplish the detection of suspected tumor image blocks for the preprocessed stained tissue areas.

The working process of the Sliding Detector modular is as follows: in the first, the image blocks are obtained from the stained tissue areas by OVERLAP strategy. Then, the

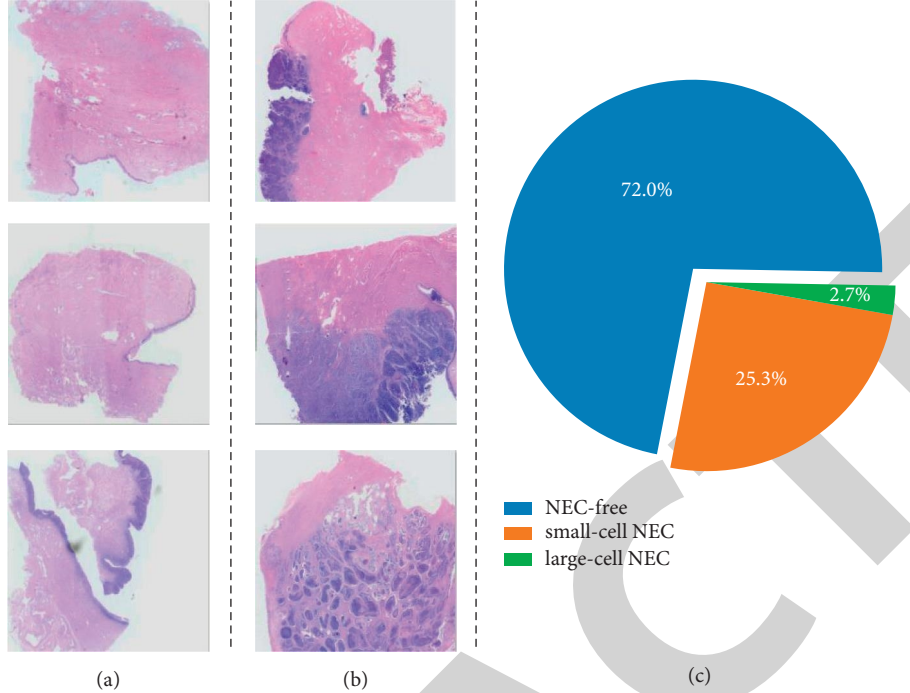


FIGURE 2: NEC dataset. (a) Examples of WSIs corresponding to three NEC-free cases. (b) Examples of WSIs corresponding to three NEC cases. (c) The proportions of various categories, both small-cell NEC and large-cell NEC, are involved in the dataset.

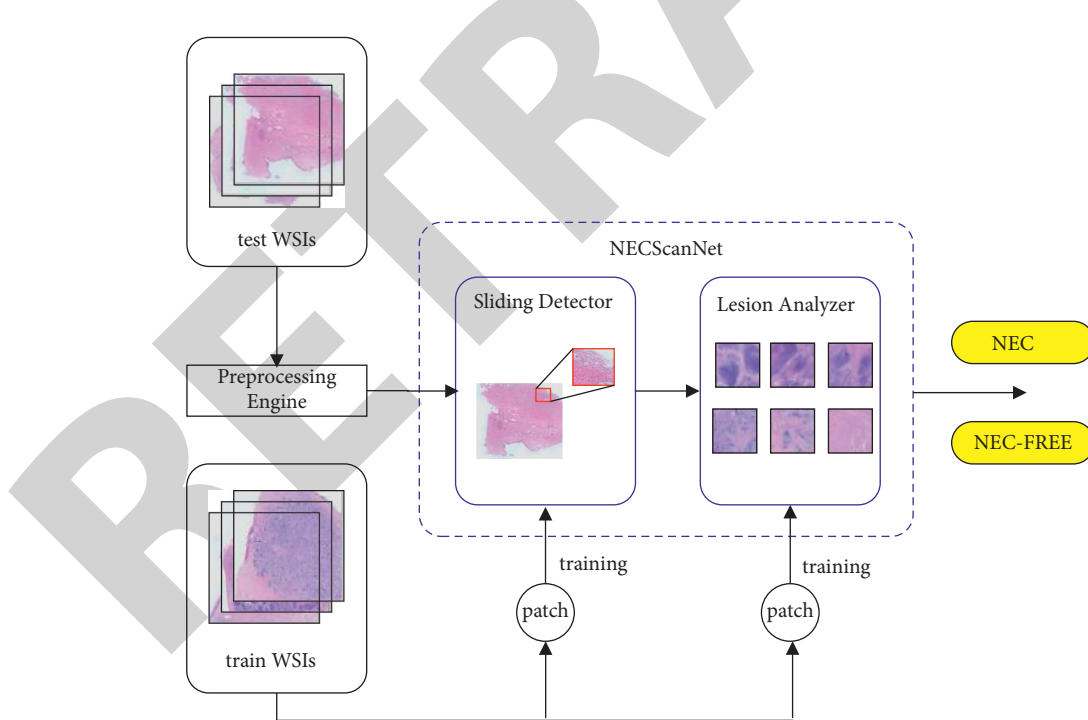


FIGURE 3: The network structure of NECSanNet, in which the Sliding Detector and Lesion Analyzer are trained individually.

category label is predicted for each image block, and then K image blocks with the highest possibilities to be tumor regions are then outputted. In the process, for the prediction of image blocks, two networks, the light weight classification network (LCN) and heavy weight classification network

(HCN), are used at the same time for the prediction of image blocks, in order to promote the feature learning capability and improve the prediction performance by taking into account both the low-order features and high-order features in the images. In this experiment, we use RESNET-50 model

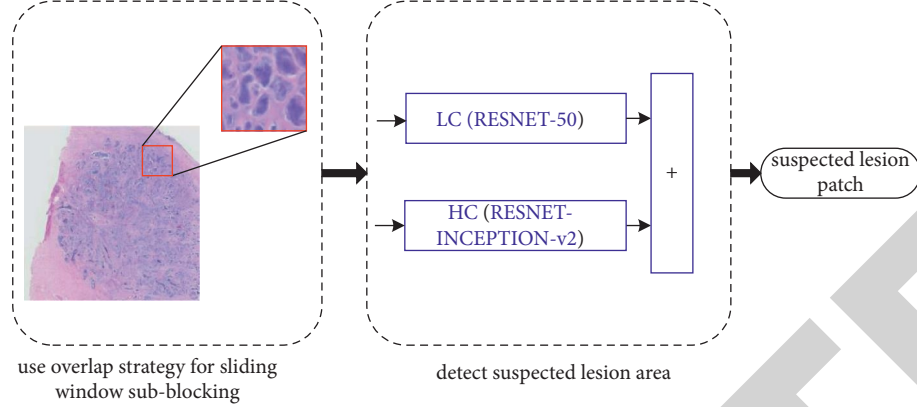


FIGURE 4: The network structure of Sliding Detector module.

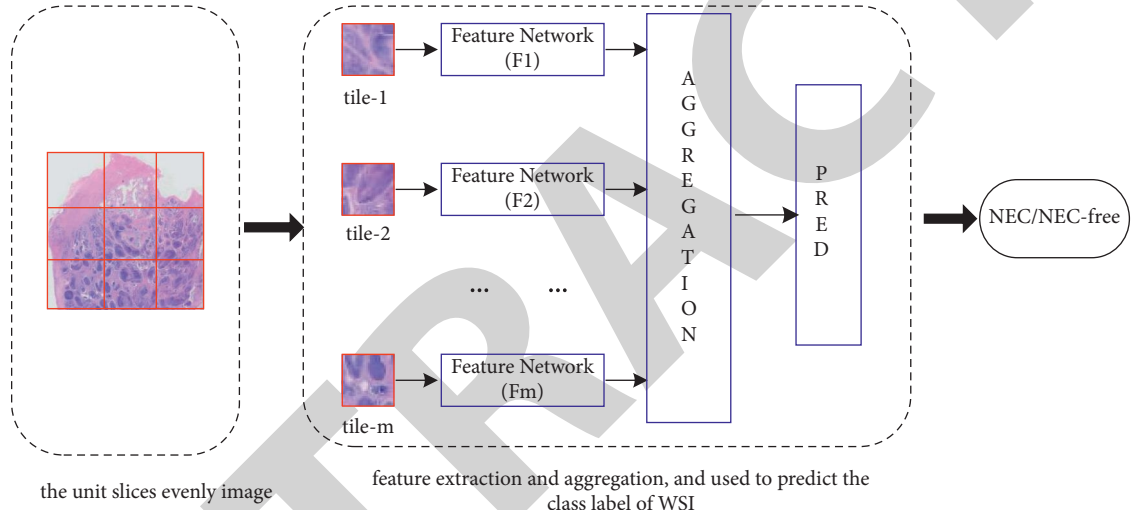


FIGURE 5: The network structure of Lesion Analyzer module.

as LCN and RESNET-INCEPTION-v2 model as HCN. The determination rules of the module for the possibilities of suspected tumor image blocks are shown in

$$\begin{cases} P_{LCN}(patch_i) \geq C_{LCN}, \\ P_{HCN}(patch_i) \geq C_{HCN}, \\ \text{MAX}_{\text{top-}K_1}(P_{LCN}(patch_i) + P_{HCN}(patch_i)), \end{cases} \quad (3)$$

in which $P_{LCN}(patch_i) \geq C_{LCN}$ represents the confidence $P_{LCN}(patch_i)$ of the image blocks to be tumor category identified by the network which is no less than the threshold C_{LCN} , $P_{HCN}(patch_i) \geq C_{HCN}$ represents the confidence $P_{HCN}(patch_i)$ of no. i image block to be tumor category identified by the HCN network which is no less than C_{HCN} , while $\text{MAX}_{\text{top-}K_1}(\bullet)$ represents the selection of the K_1 image blocks corresponding to the K_1 highest values in (3).

3.2.2. The Lesion Analyzer Module. The structure of Lesion Analyzer module is demonstrated in Figure 5. In this module, the category predictions of WSI images focused on

suspected tumor patches are accomplished by multi-instance deep learning method, and the category labels include NEC and NEC-free.

The prediction process of Lesion Analyzer is as follows: for each suspected tumor patch, the uniform blocking strategy is adopted at first to obtain the image tile set $\{\text{tile-}i\}$, and then the image tiles are input into the corresponding feature extraction network FN_i for feature extraction and followed by the feature aggregations, based on which the predictions of category labels of WSI images are accomplished. In this module, m feature extraction networks $\{FN_i\}$ are applied for feature extraction of image tiles, and the number of networks (m) is the same as the number of image tiles, in order to retain the recognition ability of meticulous and detail features, and, at the same time, to take account of the overall characteristics of suspected tumor patches. In the experiment, the improved RESNET-50 module is applied for feature extraction, and the network structure is demonstrated in Figure 6.

The category determination method for WSI images in Lesion Analyzer module is demonstrated in

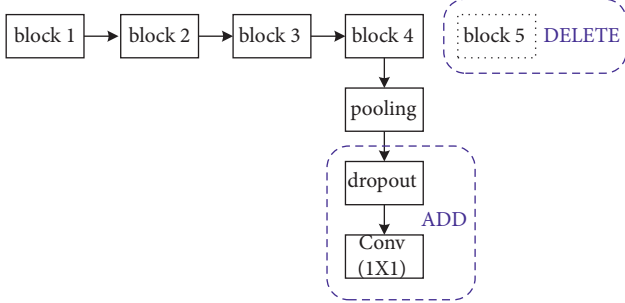


FIGURE 6: Feature network (Fm): improved residual network based on RESNET-50.

$$\sum_{i \in \text{top}-K_2} \left(\text{MAX}_{\text{top}-K_2}(P(\text{patch}_i)) \right) \geq T_{\text{lesion}}. \quad (4)$$

$\text{MAX}_{\text{top}-K_2}(\bullet)$ represents the first K_2 maximum values in (4), $P(\text{patch}_i)$ represents the confidence of suspected tumor patchpatch_i, $\sum_{i \in \text{top}-K_2}(\bullet)$ represents the sum of formula (4), and T_{lesion} represents the threshold of confidence.

4. Experiments and Results

4.1. Experimental Settings. In the NECSanNet, the Sliding Detector module $M_{\text{sliding}}(\theta_s)$ and the Lesion Analyzer module $M_{\text{analyzor}}(\theta_a)$ need to be trained separately. The image patches extracted from WSIs ($\times 40$ magnification) with 512×512 pixels are applied in the training of sliding detector module, while for the training of lesion-analyzed module, the image patches extracted from WSIs ($\times 200$ magnification) with 512×512 pixels are applied. If there is a deficiency in a certain type of images, the data augmentation is performed by rotating the image patches in 90° , 180° , and 270° .

The three-fold validation is performed in the experiment, 200 WSIs (including 144 NEC-free and 56 NEC WSIs) are applied as training set each time, and 100 WSIs (including 72 NEC-free and 28 NEC WSIs) are applied as test set. The default value of K_1 which is the number of suspected lesion regions is set to be 10, and the confidence threshold C_{LCN} for LCN network is set to be 0.5 and the same as the confidence threshold C_{HCN} for HCN network. In the Lesion Analyzer module $M_{\text{analyzor}}(\theta_a)$, the value of K_2 is 6 which represents the first 6 maximum values, and the confidence threshold C_{HCN} is set to be 0.7. All the above network parameters can be optimized by the ADAM algorithm [29], with the adaptive learning rate of 0.0001 set and the super parameter β_1 of 0.9 and β_2 of 0.9999 set.

During the experiment, the hardware configuration of the server is as follows: four 24 GB Titans RTX (GPU), Intel Xeon Silver 4114 (CPU), 125 GB memory.

4.2. NEC Screening Experiment. In order to compare the performance of the above methods and the pathologists, the evaluation indexes include *accuracy*, *precision*, and *recall* [35] are applied, which are defined by (5)–(7). The ranges of the three indexes, which are TP, TN, and FN, are all $[0, 1]$.

The higher the value, the better the performance of the module. *TP* represents the true positive sample, *TN* represents the true negative sample, *FP* represents the false positive sample, and *FN* represents the false negative sample.

$$\text{accuracy} = \frac{\text{TP} + \text{TN}}{\text{P} + \text{N}}. \quad (5)$$

In (5), *accuracy* represents the correct classification ratio among all the classified samples (positive samples *P* and negative samples *N*).

$$\text{precision} = \frac{\text{TP}}{\text{TP} + \text{FP}}. \quad (6)$$

In (6), *precision* represents the proportion of positive samples *TP* classified correctly by the module in all classified positive samples (*TP* + *FP*).

$$\text{recall} = \frac{\text{TP}}{\text{TP} + \text{FN}}. \quad (7)$$

In (7), *recall* represents the proportion of the positive samples *TP* classified correctly by the model in all the positive samples (*TP* + *FN*).

Table 1 gives results of the NEC and NEC-free decisions from both the proposed method and the diagnosis of pathologists. The first column shows types of methods, where P-J1 and P-J2 represent the diagnosis made by two junior pathologists; P-S1 and P-S2 represent the diagnosis made by two senior pathologists; SD-LA-1 represents the method in this paper without the exclusion of blank areas and interference areas by the preprocessing; SD-LA-2 represents the method in this paper but without the recommendation of suspected tumor regions by the Sliding Detector module; and SD-LA-3 represents the whole process of the method in this paper. (mean, std) in Table 1 is the mean and the standard deviation (*std*) of various indexes determined by three-fold cross validation [36].

As is demonstrated in Table 1, the whole process of the method in this paper, SD-LA-3 has a performance approximately close to the two senior pathologists (the indexes of evaluation include the mean and the mean square difference of the *accuracy*, *precision*, and *recall* obtained by the three-fold cross validation experiment), which is superior to the performance of junior pathologists. Especially, it has been confirmed by the results that SD-LA-3 has a superior performance to SD-LA-1 and SD-LA-2, providing an experimental evidence for the necessity of the preprocessing (removal of blank areas and interference areas) step and suspected tumor region recommendation by Sliding Detector module.

4.3. Comparison of the Performances in NEC Screening between the NECSanNet and the Pathologists. For the in-depth and intuitive display of the NEC screening performance, we compared and analyzed the NEC screening results of the proposed methods, junior pathologists and senior pathologists, as is shown in Figures 7 and 8.

Figure 7 demonstrates the comparison of the performance of junior pathologists (P-J1, P-J2), senior pathologists

TABLE 1: Comparison of the performances in NEC screening by junior pathologists, senior pathologists, and the proposed method. Each result shows the mean and the standard deviation determined by the three-fold cross validation (mean, standard deviation).

Method	Recall	Accuracy	Precision
P-J1	(0.738, 0.054)	(0.777, 0.021)	(0.580, 0.033)
P-J2	(0.762, 0.054)	(0.790, 0.026)	(0.598, 0.037)
P-S1	(0.941, 0.020)	(0.947, 0.012)	(0.878, 0.019)
P-S2	(0.964, 0.036)	(0.953, 0.006)	(0.881, 0.014)
SD-LA-1	(0.750, 0.071)	(0.703, 0.046)	(0.482, 0.052)
SD-LA-2	(0.607, 0.036)	(0.693, 0.050)	(0.493, 0.035)
SD-LA-3	(0.929, 0.036)	(0.927, 0.015)	(0.830, 0.021)

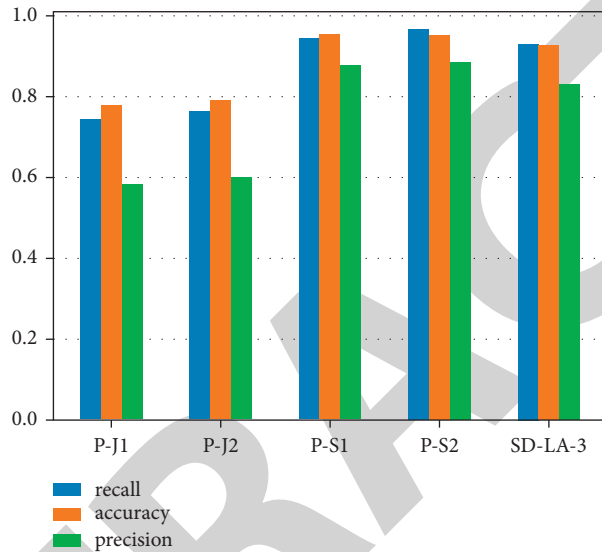


FIGURE 7: The comparison of three-fold cross validation results for the proposed method and pathologists in NEC screening.

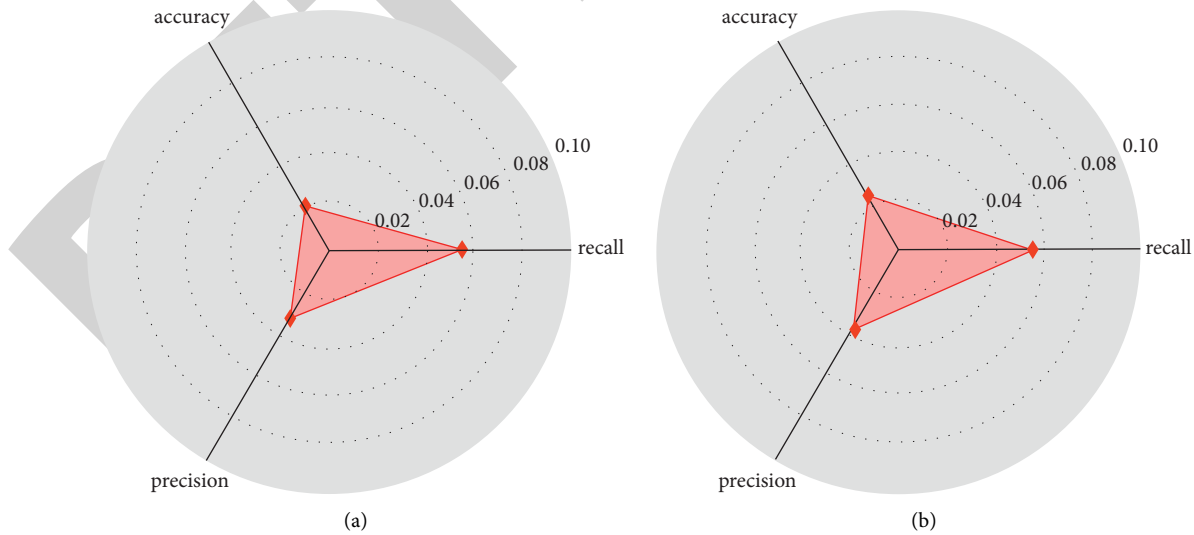


FIGURE 8: Continued.

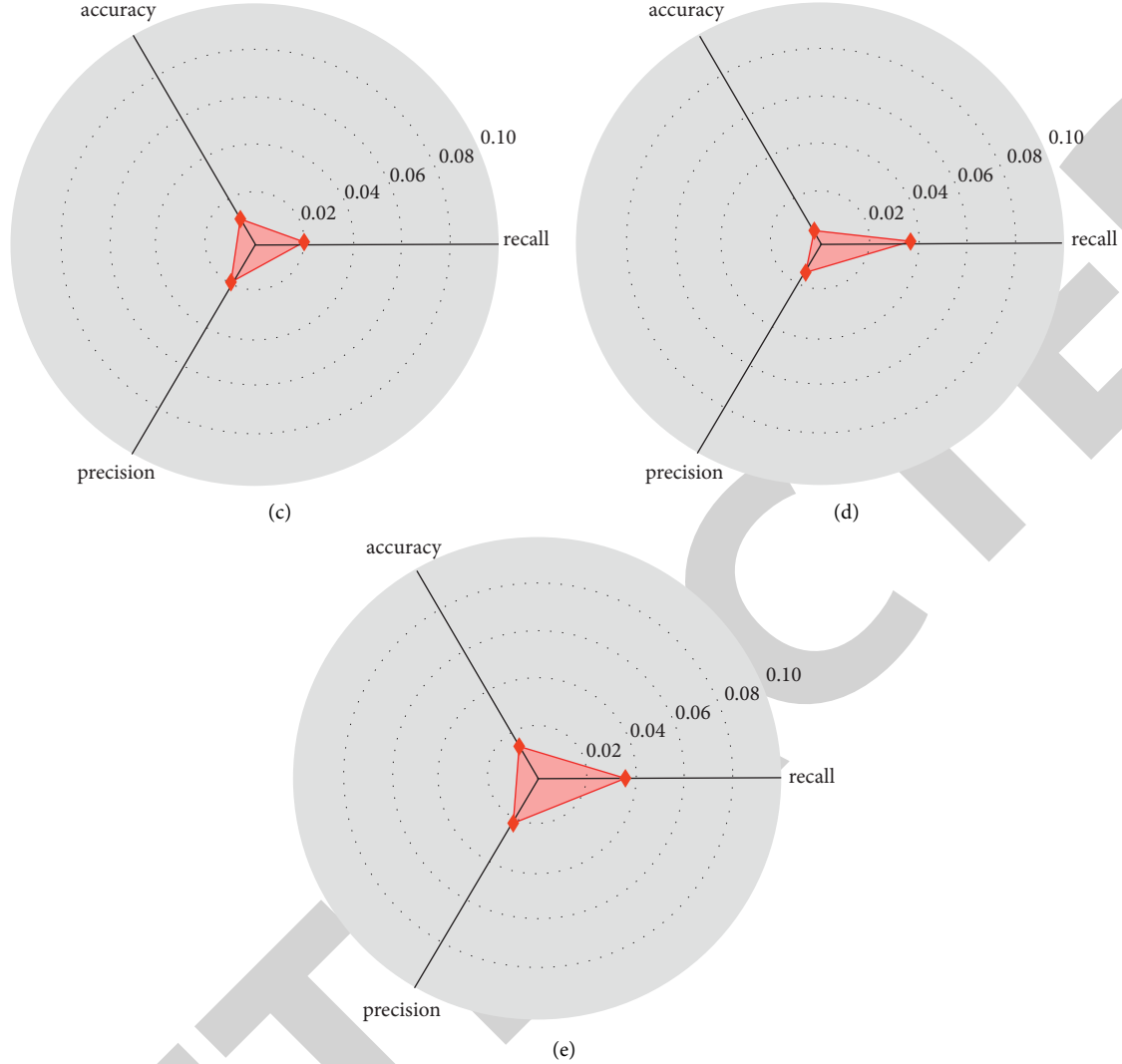


FIGURE 8: The comparison of mean square deviations in three-fold cross validations for the proposed method and pathologists in NEC screening. (a) P-J1, (b) P-J2, (c) P-S1, (d) P-S2, and (e) SD-LA-3.

(P-S1, P-S2), and the proposed method (SD-LA-3) validated by three-fold cross validation. The height of the rectangle in the figure represents the mean value in this group. It can be noticed that the recall, accuracy, and precision of the proposed method SD-LA-3 are all superior than those of junior pathologists (P-J1, P-J2) and close to those of senior pathologists (P-S1, P-S2).

Figure 8 demonstrates the mean square deviations of recall, accuracy, and precision for the proposed method and pathologists in NEC screening, which prove the stability of performance. It is obvious in the figure that the mean square deviations of the three indexes for the proposed method (SD-LA-3) are all much lower than the junior pathologists (P-J1, P-J2) and slightly lower than the senior pathologists (P-S1, P-S2), indicating that the stability of the proposed method in NEC screening is slightly better than the senior pathologists and apparently superior than the junior pathologists.

4.4. Ablation Study. Additional ablation studies are conducted to validate our design choices, and the results are demonstrated in Figures 9 and 10. Specially, in order to verify the necessity and effectiveness of each intermediate step involved in the proposed method, the NEC screening tests are also performed by SD-LA-1 which represents the proposed method without the step of preprocessing for blank and interfered region exclusions and SD-LA-2 which represents the proposed method without the step of Sliding Detector module, and their performances analyzed by three-fold validations are compared with SD-LA-3 which represents the whole process of the proposed method, and the results are demonstrated in Figures 9 and 10.

It can be seen that the average values of recall, accuracy, and precision of SD-LA-3 are all obviously higher than those of SD-LA-1 and SD-LA-2 (Figure 10), while the mean square deviations of the three indexes for SD-LA-3 (Figure 10(c)) are significantly lower than those of SD-LA-1 (Figure 10(a))

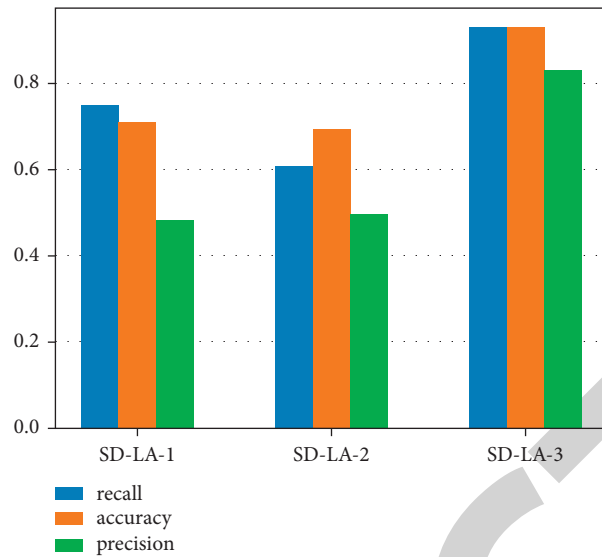


FIGURE 9: The comparison of results in three-fold cross validation for SD-LA-1, SD-LA-2, and SD-LA-3.

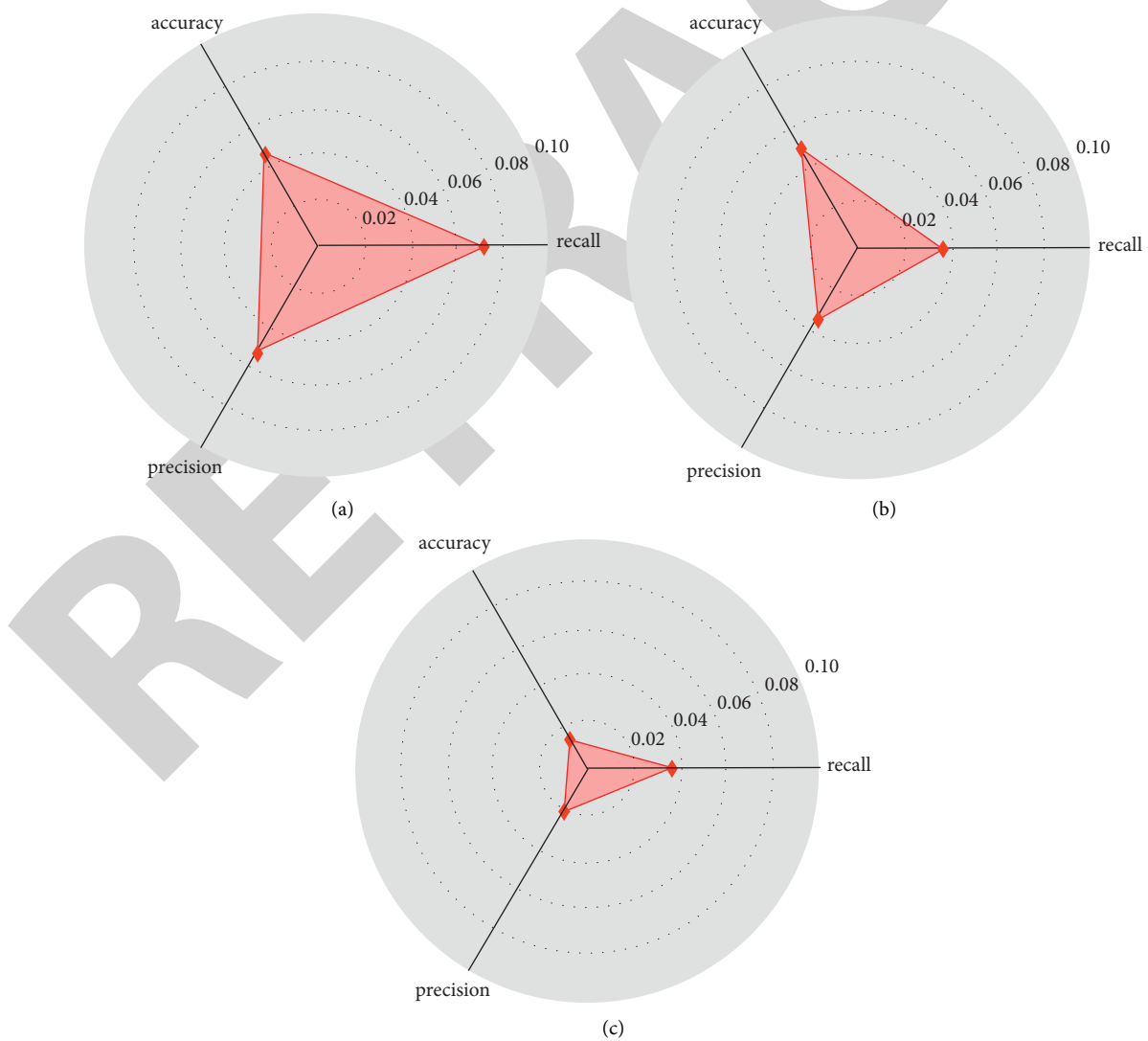


FIGURE 10: The comparison of mean square deviations in three-fold cross validations for (a) SD-LA-1, (b) SD-LA-2, and (c) SD-LA-3.

TABLE 2: Examples of NEC diagnosis.

WSIs	Ground truth	P-J1	P-J1	P-S1	P-S2	SD-LA-3
	NEC-free	NEC-free	NEC-free	NEC-free	NEC-free	NEC-free
	NEC-free	NEC	NEC-free	NEC-free	NEC-free	NEC-free
	NEC	NEC	NEC	NEC	NEC	NEC
	NEC	NEC	NEC-free	NEC	NEC	NEC
	NEC	NEC-free	NEC-free	NEC	NEC	NEC-free

and SD-LA-2 (Figure 10(b)). The results demonstrate that the preprocessing (removal of blank and interfered regions) and Sliding Detector module (detection of suspected lesion regions) cannot just promote the recall, accuracy, and precision of the proposed method in NEC screening but also improve the stability of performance, providing evidences to the necessities of the two intermediate steps.

4.5. Screening Results of Some Typical Cases. The prognosis analysis results of WSIs corresponding to six cases are shown in Table 2, in which the first column shows the H&E staining pathological WSIs of these cases, the second column shows the real status of the cases (NEC/NEC-free), the diagnosis of four pathologists (two junior pathologists and two senior pathologists) is demonstrated from the third column to the sixth column. The seventh column shows the diagnosis of the proposed method in this paper. It can be seen from Tables 1 and 2 that under the experimental conditions described in Section 4.1, the method proposed in this paper has a higher *accuracy* and *recall* than junior pathologist and a performance approximate to the senior pathologists. The conclusions above demonstrate the effectiveness of the proposed method for the intelligent diagnosis of NEC.

5. Conclusions

In this paper, a new multi-instance deep model is applied to detect cervical NEC on the pathological WSIs, in order to assist in the pathological diagnosis. With this method, the pathological WSIs can be applied and analyzed directly by

the mainstream computer vision model without the reduction of image pixels; meanwhile, the combination of Sliding Detector module and Lesion Analyzer module successfully addresses the problem of NEC detection on WSIs and the performance of the model demonstrates a great potential in the computer-assisted diagnosis of cervical NEC which is worth of further investigations in the practical diagnostic scene to verify its value. The application of computer-assisted diagnosis in the rare malignancy highlights the importance of cooperation between medical specialists and computer scientists and also the broad future of artificial intelligence in the medical field to help with the pathological diagnosis of complicated diseases.

Data Availability

The data used to support the findings of this study are available from the corresponding author upon request.

Conflicts of Interest

The authors declare that they have no known competing financial interests or personal relationships that could have appeared to influence the work reported in this paper.

Authors' Contributions

Conceptualization was performed by Xin Liao; methodology was developed by Xin Liao and Xin Zheng; validation was performed by Qin Huang; formal analysis was performed by Qin Huang; data curation was performed by Xin Liao and Qin Huang; original draft was written by Xin Liao and Xin

Zheng; writing review and editing is carried out by Xin Liao and Qin Huang; funding was acquired by Xin Liao. All the authors have read and agreed to the published version of the manuscript.

Acknowledgments

This study was supported by the Research on Expert Knowledge Base for Automatic Diagnosis of Cervical Pathology Based on Big Data Deep Learning (2017LF3008). This research was supported by the grants from Key Laboratory Open Foundation of Sichuan Province .

References

- [1] B. Yoseph, M. Chi, A. M. Truskinovsky, and A. Z. Dudek, "Large-cell neuroendocrine carcinoma of the cervix," *Rare Tumors*, vol. 4, no. 1, pp. 58–60, 2012.
- [2] J. K. C. Chan, W. M. S. Tsui, S. Y. Tung, and R. C. T. Ching, "Endocrine cell hyperplasia of the uterine cervix: a precursor of neuroendocrine carcinoma of the cervix?" *American Journal of Clinical Pathology*, vol. 92, no. 6, pp. 825–830, 1989.
- [3] C. Gilks, R. Young, D. Gersell, and P. Clement, "Large cell neuroendocrine [corrected] carcinoma of the uterine cervix: a clinicopathologic study of 12 cases," *The American Journal of Surgical Pathology*, vol. 21, no. 8, pp. 905–914, 1997.
- [4] M. H. Stoler, S. E. Mills, D. J. Gersell, and A. N. Walker, "Small-cell neuroendocrine carcinoma of the cervix," *The American Journal of Surgical Pathology*, vol. 15, no. 1, pp. 28–32, 1991.
- [5] B. A. Margolis, J. D. Wright, L. Chen, J. Y. Hou, A. I. Tergas, and W. M. Burke, "Neuroendocrine carcinoma of the cervix: poor survival despite aggressive treatment at all stages," *Gynecologic Oncology*, vol. 141, p. 84, 2016.
- [6] S. Kuntz, E. Krieghoff-Henning, J. N. Kather et al., "Gastrointestinal cancer classification and prognostication from histology using deep learning: systematic review," *European Journal of Cancer*, vol. 155, pp. 200–215, 2021.
- [7] Y. Hou, "Breast cancer pathological image classification based on deep learning," *Journal of X-Ray Science and Technology*, vol. 28, no. 4, pp. 727–738, 2020.
- [8] S. Zhang, Z. Yuan, Y. Wang, Y. Bai, B. Chen, and H. Wang, "REUR: a unified deep framework for signet ring cell detection in low-resolution pathological images," *Computers in Biology and Medicine*, vol. 136, Article ID 104711, 2021.
- [9] L. Wang, L. Ding, Z. Liu et al., "Automated identification of malignancy in whole-slide pathological images: identification of eyelid malignant melanoma in gigapixel pathological slides using deep learning," *British Journal of Ophthalmology*, vol. 104, no. 3, pp. 318–323, 2020.
- [10] Y. H. Qu, H. T. Zhu, K. Cao, X. T. Li, M. Ye, and Y. S. Sun, "Prediction of pathological complete response to neoadjuvant chemotherapy in breast cancer using a deep learning (DL) method," *Thoracic Cancer*, vol. 11, no. 3, pp. 651–658, 2020.
- [11] F. Zhang, L. Z. Zhong, X. Zhao, D. Dong, and H. Shan, "A deep-learning-based prognostic nomogram integrating microscopic digital pathology and macroscopic magnetic resonance images in nasopharyngeal carcinoma: a multi-cohort study," *Therapeutic Advances in Medical Oncology*, vol. 12, 2020.
- [12] J. Schmidhuber, "Deep learning in neural networks: an overview," *Neural Networks*, vol. 61, pp. 85–117, 2015.
- [13] Z. Niu, G. Zhong, and H. Yu, "A review on the attention mechanism of deep learning," *Neurocomputing*, vol. 452, pp. 48–62, 2021.
- [14] E. Sudheer Kumar and C. Shoba Bindu, "Medical image analysis using deep learning: a systematic literature review," in *Proceedings of the Emerging Technologies in Computer Engineering: Microservices in Big Data Analytics*, pp. 81–97, Jaipur, India, February 2019.
- [15] X. Fei, L. Shen, S. Ying et al., "Parameter transfer deep neural network for single-modal B-mode ultrasound-based computer-aided diagnosis," *Cognitive Computation*, vol. 12, no. 7, pp. 1–13, 2020.
- [16] H. H. N. Pham, M. Futakuchi, A. Bychkov, T. Furukawa, K. Kuroda, and J. Fukuoka, "Detection of lung cancer lymph node metastases from whole-slide histopathologic images using a two-step deep learning approach," *American Journal Of Pathology*, vol. 189, no. 12, pp. 2428–2439, 2019.
- [17] G. Campanella, M. G. Hanna, L. Geneslaw et al., "Clinical-grade computational pathology using weakly supervised deep learning on whole slide images," *Nature Medicine*, vol. 25, no. 8, pp. 1301–1309, 2019.
- [18] P. Mehta, M. Antonelli, H. U. Ahmed, M. Emberton, S. Punwani, and S. Ourselin, "Computer-aided diagnosis of prostate cancer using multiparametric MRI and clinical features: a patient-level classification framework," *Medical Image Analysis*, vol. 73, Article ID 102153, 2021.
- [19] H. Lu, "Computer-aided diagnosis research of a lung tumor based on a deep convolutional neural network and global features," *BioMed Research International*, vol. 2021, Article ID 5513746, 12 pages, 2021.
- [20] A. Saygili, "A new approach for computer-aided detection of coronavirus (COVID-19) from CT and X-ray images using machine learning methods," *Applied Soft Computing*, vol. 105, Article ID 107323, 2021.
- [21] G. Lemaître, R. Martí, J. Freixenet, J. C. Vilanova, P. M. Walker, and F. Meriaudeau, "Computer-Aided Detection and diagnosis for prostate cancer based on mono and multi-parametric MRI: a review," *Computers in Biology and Medicine*, vol. 60, pp. 8–31, 2015.
- [22] R. S. Alomari, J. J. Corso, V. Chaudhary, and G. Dhillon, "Computer-aided diagnosis of lumbar disc pathology from clinical lower spine MRI," *International Journal of Computer Assisted Radiology and Surgery*, vol. 5, no. 3, pp. 287–293, 2010.
- [23] M. Al-Antari, C. H. Hua, J. Bang, and S. Lee, "Fast deep learning computer-aided diagnosis of COVID-19 based on digital chest x-ray images," *Applied Intelligence*, vol. 6, pp. 1–18, 2020.
- [24] C. Chu, J. Zheng, and Y. Zhou, "Ultrasonic thyroid nodule detection method based on U-Net network," *Computer Methods and Programs in Biomedicine*, vol. 199, Article ID 105906, 2020.
- [25] M. Zhu, Z. Chen, and Y. Yuan, "DSI-net: deep synergistic interaction network for joint classification and segmentation with endoscope images," *IEEE Transactions on Medical Imaging*, vol. 5, pp. 1–11, 2021.
- [26] R. Subramanian, S. Guptha, R. Devika Rubi, A. Krishna Kasavaraju, and S. Jain, "Automatic classification of sentinel lymph node (SLN) metastases in breast carcinoma whole slide image (WSI) through densenet deep learning network," *IP Journal of Diagnostic Pathology and Oncology*, vol. 5, no. 2, pp. 144–150, 2020.
- [27] A. Pc, L. A. Yun, A. Xs, Y. A. Lin, and B. Pg, "Automatic whole slide pathology image diagnosis framework via unit stochastic

- selection and attention fusion,” *Neurocomputing*, vol. 453, pp. 312–325, 2021.
- [28] J. Yao, X. Zhu, J. Jonnagaddala, N. Hawkins, and J. Huang, “Whole slide images based cancer survival prediction using attention guided deep multiple instance learning networks,” *Medical Image Analysis*, vol. 65, Article ID 101789, 2020.
- [29] Y. Yang, Y. Yang, Y. Yuan, J. Zheng, and Z. Zhongxi, “Detecting helicobacter pylori in whole slide images via weakly supervised multi-task learning,” *Multimedia Tools and Applications*, vol. 79, no. 35-36, pp. 26787–26815, 2020.
- [30] P. Teeffey, B. Orr, M. Vogt, and W. Roberts, “Neuroendocrine carcinoma of the cervix during pregnancy: a case report,” *Gynecologic Oncology Case Reports*, vol. 2, no. 3, pp. 73-74, 2012.
- [31] C. Baykal, A. Al, G. Tulunay et al., “High-grade neuroendocrine carcinoma of the cervix,” *Gynecologic and Obstetric Investigation*, vol. 59, no. 4, pp. 207–211, 2005.
- [32] Q. Bi, K. Qin, Z. Li, H. Zhang, K. Xu, and G. S Xia, “A multiple-instance densely-connected ConvNet for aerial scene classification,” *IEEE Transactions on Image Processing: A Publication of the IEEE Signal Processing Society*, vol. 29, pp. 4911–4925, 2020.
- [33] H. Yang, L. Chen, Z. Cheng et al., “Deep learning-based six-type classifier for lung cancer and mimics from histopathological whole slide images: a retrospective study,” *BMC Medicine*, vol. 19, no. 1, p. 80, 2021.
- [34] T. Vu, P. Lai, R. Raich, A. Pham, and U. A. Rao, “A novel attribute-based symmetric multiple instance learning for histopathological image analysis,” *IEEE Transactions on Medical Imaging*, vol. 39, p. 1, 2020.
- [35] J. T. Townsend, “Erratum to: theoretical analysis of an alphabetic confusion matrix,” *Perception & Psychophysics*, vol. 10, no. 4, p. 256, 1971.
- [36] B. Efron, “Estimating the error rate of a prediction rule: improvement on cross-validation,” *Journal of the American Statistical Association*, vol. 78, no. 382, pp. 316–331, 1983.